JACS
JOURNAL OF THE AMERICAN CHEMICAL SOCIETY
Article
pubs.acs.org/JACS

In Situ Coupling of Strung Co_4N and Intertwined N–C Fibers toward Free-Standing Bifunctional Cathode for Robust, Efficient, and Flexible Zn–Air Batteries

Fanlu Meng,[†,‡] Haixia Zhong,[†,§] Di Bao,[†] Junmin Yan,[‡] and Xinbo Zhang*[,†]

[†]State Key Laboratory of Rare Earth Resource Utilization, Changchun Institute of Applied Chemistry, Chinese Academy of Sciences, Changchun 130022, Jilin, China

[‡]Key Laboratory of Automobile Materials, Ministry of Education and College of Materials Science and Engineering, Jilin University, Changchun 130012, Jilin, China

[§]University of Chinese Academy of Sciences, Beijing 100049, China

Supporting Information

ABSTRACT: Flexible power sources with high energy density are crucial for the realization of next-generation flexible electronics. Theoretically, rechargeable flexible zinc–air (Zn–air) batteries could provide high specific energy, while their large-scale applications are still greatly hindered by high cost and resources scarcity of noble-metal-based oxygen evolution reaction (OER)/oxygen reduction reaction (ORR) electrocatalysts as well as inferior mechanical properties of the air cathode. Combining metallic Co_4N with superior OER activity and Co–N–C with perfect ORR activity on a free-standing and flexible electrode could be a good step for flexible Zn–air batteries, while lots of difficulties need to be overcome. Herein, as a proof-of-concept experiment, we first propose a strategy for in situ coupling of strung Co_4N and intertwined N–C fibers, by pyrolyzation of the novel pearl-like ZIF-67/polypyrrole nanofibers network rooted on carbon cloth. Originating from the synergistic effect of Co_4N and Co–N–C and the stable 3D interconnected conductive network structure, the obtained free-standing and highly flexible bifunctional oxygen electrode exhibits excellent electrocatalytic activity and stability for both OER and ORR in terms of low overpotential (310 mV at 10 mA cm^{-2}) for OER, a positive half-wave potential (0.8 V) for ORR, and a stable current density retention for at least 20 h, and especially, the obtained Zn–air batteries exhibit a low discharge–charge voltage gap (1.09 V at 50 mA cm^{-2}) and long cycle life (up to 408 cycles). Furthermore, the perfect bendable and twistable and rechargeable properties of the flexible Zn–air battery particularly make it a potentially power portable and wearable electronic device.

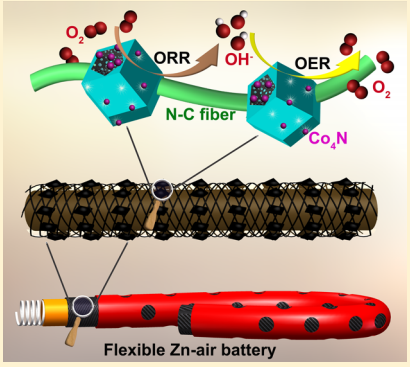

1. INTRODUCTION

Flexible electronics, due to their unique advantages including being bendable, portable, foldable, and potentially wearable, have revolutionized many industries ranging from consumer products, automotive, and aerospace to medical.[1,2] To fulfill "flexible electronics" society, well-matched flexible energy storage/conversion devices must be developed as a key component. Theoretically, zinc–air batteries are suitable to power flexible electronics due to advantages of having high energy density (1086 Wh kg^{-1}, including oxygen)[3] and low cost and being environmentally friendly. However, conventional Zn–air batteries are typically flat and rigid and thus cannot meet the requirements of portable and wearable devices. Although significant processes have been achieved in improving the flexibility, stretchability, and wearability of Zn–air batteries, the obtained electrochemical performances are still far from satisfying because the energy efficiency is still limited by the large overpotentials derived from the sluggish oxygen reduction and evolution reactions (ORR/OER) kinetics,[4] the unstable electrode structure even further fueling it. Therefore, the development of novel air electrode with high catalytic activity, good conductivity, and favorable mechanical properties, such as flexibility and stretchability, is of great importance.

Up to now, the benchmark catalysts for ORR and OER are Pt-based and Ir/Ru-based compounds, respectively; however, the high cost and scarcity terribly impede their widespread applications.[5] In response, many research efforts have been devoted to developing novel and efficient ORR/OER electrocatalysts, based on earth abundant and inexpensive elements to replace this noble metal, including transition metal oxides,[5b,6] sulfides,[7] and carbons.[8] Although significant progresses have been made, very few electrocatalysts are highly active toward both ORR and OER. Such bifunctional electrocatalysts are significantly attractive because avoiding using different equipment and processes to produce different electrocatalysts could decrease the cost. Normally, a general strategy to improve the oxygen (ORR/OER) electrode performance is fabrication of

Received: May 16, 2016
Published: July 27, 2016

DOI: 10.1021/jacs.6b05046
J. Am. Chem. Soc. 2016, 138, 10226–10231

nanostructured catalysts and then dispersing the catalysts on conducting substrate. However, the possible mechanical shedding from the polymer binder and/or supporting materials would lead to catalyst degradation. Furthermore, the polymeric binders are generally inactive and insulating, which would inevitably induce the reduction of capacity and increase of manufacturing costs of batteries.[9]

In response, building a binder-free electrode based on highly efficient bifunctional ORR/OER electrocatalysts and a three-dimensional (3D) skeleton can simultaneously meet these essential challenges.[10] Metallic Co_4N holds superior OER activity because it overcomes intrinsically inferior electrical conductivity of semiconducting Co-based oxides,[11] while its ORR activity is rather poor due to the inherent nature of Co-based materials.[12] Theoretically, combination Co_4N with ORR active Co−N−C (transition metal (Fe or Co, etc.)−N coordination sites have been generally considered to be the most promising substitutes for Pt-based catalysts) could be a good step for Co_4N toward bifunctional OER/ORR electrocatalysts; however, how to bridge over the huge differences of the synthesis process between them is still very challenging (the incompatible Co precursors and synthesis conditions).[13,14] Particularly, when going extra miles, it is still a big challenge to fabricate them as free-standing and flexible electrode necessarily required as air cathode for flexible Zn−air batteries. Therefore, it is urgent to design a 3D free-standing bifunctional OER/ORR electrode for flexible Zn−air battery, taking advantage of the noble-metal-free Co_4N and Co−N−C.

Herein, as a proof-of-concept experiment, we first propose and demonstrate a novel and flexible 3D free-standing bifunctional electrode composed of Co_4N, carbon fibers network, and carbon cloth (Co_4N/CNW/CC), by pyrolyzation of string of ZIF-67 on polypyrrole (PPy) nanofibers network rooted on carbon cloths (ZIF-67/PNW/CC), wherein, different from the traditional extra NH_3 treatment of Co-oxides/hydroxides, the nitrogenous gases released from the pyrolysis of PPy are creatively used to promote the in situ conversion of ZIF-67 to Co_4N. The intertwined N−C fibers derived from PPy nanofibers encase carbon cloths forming a stable 3D interconnected conductive network structure. Furthermore, the unique pearl-like structure of ZIF-67/PNW makes the porous N-doped carbon species anchor Co_4N particles and Co−N−C active sites on intertwined N−C fibers, which undoubtedly ensures the stability. Benefiting from all these advantages, Co_4N/CNW/CC electrode shows excellent catalytic activity for OER and ORR, as well as exceptionally high performance for rechargeable flexible Zn−air batteries with great mechanical strength.

2. RESULTS AND DISCUSSION

Figure 1a and Figure S1 illustrate the synthesis strategy for the Co_4N/CNW/CC, which includes the electrodeposition of PPy nanofibers on carbon cloths, growth of ZIF-67 wrapped on PPy nanofibers, and final carbonization under N_2 atmosphere. Scanning electron microscopy (SEM) and transmission electron microscopy (TEM) are first employed to demonstrate the morphology and structure evolution. As shown in Figure S2, such long PPy nanofibers with an average diameter of 100 nm are interconnected with each other forming a 3D network structure, and lots of ZIF-67 particles encase the fibers looking like pearl necklaces. After thermal treatment, not only the 3D network structures, but also the polyhedral shape of the ZIF-67 nanoparticles, are retained well, proven by the SEM and TEM

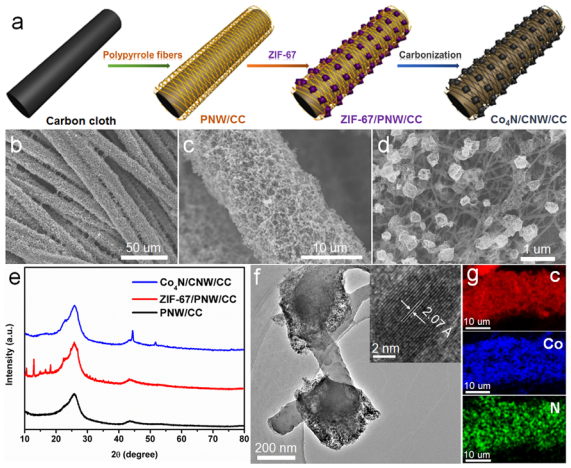

Figure 1. (a) Scheme of the synthesis of Co_4N/CNW/CC. (b−d) Low- and high-magnification SEM images of Co_4N/CNW/CC. (e) XRD patterns of PNW/CC, ZIF-67/PNW/CC, and Co_4N/CNW/CC. (f) TEM image of Co_4N/CNW/CC (inset HRTEM image of Co_4N). (g) SEM EDS element mapping of C, Co, and N for Co_4N/CNW/CC.

images in Figure 1b−d. It should be noted that the ZIF-67 derived particles consist of multiple Co_4N nanoparticles inserted into the rough and porous carbon matrices (Figure 1d and f). The numerous pores in ZIF-67 derived particles are preferably generated via deterioration and carbonization of the organic dimethylimidazole.[15] The structures are then investigated by X-ray diffraction (XRD); multiple peaks of the product match well with the pure Co_4N phase with a cubic structure, indicating the successful transformation from ZIF-67 to Co_4N (Figure 1e).[11] The high-magnification transmission electron microscopy (HRTEM) image (Figure 1f inset) shows a distinct lattice fringe of 0.207 nm, which is consistent with the (111) lattice plane of Co_4N product. Moreover, energy dispersive X-ray spectroscopy (EDS) element mapping confirms the homogeneous spatial distributions of Co_4N and carbon nanofiber networks on the carbon cloths (Figure 1g), which should be benefited from the initial uniform growth of ZIF-67 on PPy nanofibers. The nitrogen adsorption/desorption isotherm shows the mesoporous features of Co_4N/CNW/CC with the BET surface area of 226 $m^2\ g^{-1}$ and the pore volume of 0.44 $cm^3\ g^{-1}$ (Figure S3, Supporting Information). For comparison, Co_4N/CC, and CNW/CC derived from ZIF-67/carbon cloth (ZIF-67/CC), and PPy nanofibers network/carbon cloth (PNW/CC) are also synthesized, respectively. The XRD patterns in Figure S4a confirm the high crystallinity and zeolite-type structure in both ZIF-67/PNW/CC and ZIF-67/CC. Fourier-transform infrared (FTIR) spectra (Figure S4b) further illustrate the characteristic peaks of ZIF-67. After thermal treatment, the morphology of Co_4N/CC or CNW/CC is just like the fibers or particles of Co_4N/CNW/CC coating on carbon cloths (Figure S5a and S6c, Supporting Information). The mesoporous features derived from ZIF-67 are obvious in Co_4N/CC (Figure S6d). The Co_4N/CC and Co_4N/CNW/CC almost have the same diffraction peaks in XRD patterns (Figure S7a). However, the difference of Co $2p_{3/2}$ XPS date (Figure S10) between them indicates the metal Co (peak at 778 eV) in Co_4N/CC. It may be concluded that the nitrogenous gases, such as NH_3 (Figure S8), released from the pyrolysis of PPy promote the formation of Co_4N. The change of components and structures for samples prepared at other temperatures is

DOI: 10.1021/jacs.6b05046
J. Am. Chem. Soc. 2016, 138, 10226−10231

clearly reflected by SEM images (Figure S9) and XRD and XPS spectra. As shown in Figure S7b, there are almost no diffraction peaks about Co or Co_4N for the sample thermal treated at 500 °C. But, all the diffraction peaks become stronger with the increase of temperature. Co $2p_{3/2}$ XPS dates in Figure S10 identify the variation of composition caused by temperature. The peak at 779.1 eV should be related to Co−Cx for the sample at 500 °C.[16] When continuously increasing temperature from 700 to 800 °C, the peak of metal Co appears, indicating that the temperature plays the key role in the formatting of Co_4N. As indicated in Figure S11, the XPS N 1s spectra can be deconvoluted into three peaks, which are attributed to the Co−N bonding (398.9 eV),[13a,c] pyridinic-N (398.4 eV), and graphitic-N (400.5 eV)[14d] for Co_4N/CNW/CC. The positive shift of pyridinic-N (398.4 eV) in Co_4N/CNW/CC compared to that of CNW/CC (398.2 eV) may prove the existence of Co−N−C in carbon matrix. In order to eliminate the influence of Co_4N, the Co_4N/CNW/CC is etched by nitrohydrochloric acid named as Co_4N/CNW/CC-A, and no peaks about Co_4N in XRD patterns are observed in Co_4N/CNW/CC-A (Figure S12a). The positive shift of pyridinic-N (398.4 eV) and Co−Nx (Figure S12b, c) still exists, which is undoubtedly related to Co−N−C in carbon matrix. As in the case of early studies,[17] Co−N-C, derived from pyrolysis of ZIF-67, has been identified as one of the best active sites for ORR.

To verify whether Co_4N/CNW/CC could serve as a highly efficient OER electrocatalyst, it is directly applied as the working electrode for electrochemical measurements performed in 1 M KOH solution. In contrast, the Co_4N/CNW/CC is cut into very small pieces, ground into fine powder, and mixed with binder and alcohol-forming slurry. The slurry is carefully dropped on a piece of carbon cloth in the same size as the electrode (named as P−Co_4N/CNW/CC) for the OER measurements. Co_4N/CC, CNW/CC, and pure carbon cloth are also examined for comparison. We first compare the operating potentials required for different catalysts to deliver a current density of 10 mA cm^{-2}; the Co_4N/CNW/CC displays a significantly low potential (ca. 1.54 V) compared to P−Co_4N/CNW/CC (1.58 V), Co_4N/CC (1.59 V), and CNW/CC (1.63 V) as shown in Figure 2a, meaning excellent OER activity of Co_4N/CNW/CC. Among the series of samples treated at different temperatures, Co_4N/CNW/CC with 700 °C exhibits the best activity, wherein an optimal balance is maybe realized between conductivity and amount of active sites (Figure S13). The catalytic kinetics for OER is also examined by Tafel plots. As revealed in Figure 2b, the Tafel slope of Co_4N/CNW/CC is approximately 81 mV/decade, which is smaller than that of P−Co_4N/CNW/CC (113 mV/decade), Co_4N/CC (83 mV/decade), and CNW/CC (179 mV/decade), indicating a higher OER kinetics. The 3D network structures combined with ZIF-67 after carbonization creating abundant pores could provide a larger active surface area, which can be evaluated around by using the electrochemical double-layer capacitance. The Co_4N/CNW/CC reveals a capacitance of 185 mF cm^{-2}, higher than that of Co_4N/CC (79 mF cm^{-2}) and CNW/CC (66 mF cm^{-2}) (Figure S14). Ion and charge transports are other crucial factors for efficient electrocatalysts. Thus, we measured the electrochemical impedance spectroscopy (EIS). The semicircular diameter of Co_4N/CNW/CC in Figure S15 is much smaller than that of P−Co_4N/CNW/CC, implying lower resistance. To assess the OER stability of Co_4N/CNW/CC, 1000 continuous potential cycles and a chronoamperometric test are carried out. The polarization curve achieved after 1000 cycles shows very small decline (Figure 2c). Meanwhile, the strong activity maintenance over 20 h further suggests the long-term durability (Figure 2d). In contrast, for the P−Co_4N/CNW/CC, the catalytic activity or stability is much lower than that of Co_4N/CNW/CC. The XPS Co $2p_{3/2}$ spectra of Co_4N/CNW/CC after a 20 h reaction recognize the oxides with Co−N bonding (Figure S16a), which should own to the surface oxidation. As explained by the earlier report,[11] oxides on the surface of Co_4N act as the real OER active sites, whereas the XRD pattern after cycle still shows the peaks of Co_4N, proving the stable core metallic Co_4N (Figure S16b). Based on these results, the Co_4N/CNW/CC exerts high OER activity which is comparable to commercial RuO_2 and exhibits much better stability (Figure S17). All the results above in fact suggest the enormous advantages of the 3D binder-free electrode, such as high electronic conductivity, abundant pores with larger active surface area, and more efficient gas transport.

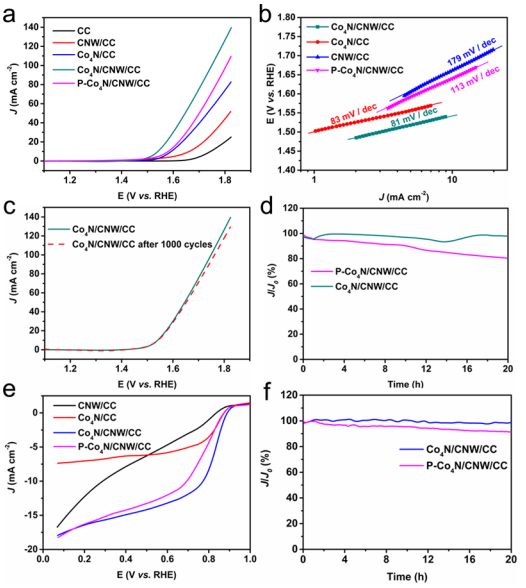

Figure 2. (a) OER polarization curves of Co_4N/CNW/CC, P−Co_4N/CNW/CC, Co_4N/CC, CNW/CC, and CC (at the scanning rate of 5 mV s^{-1} in 1 M KOH solution). (b) Tafel plots of Co_4N/CNW/CC, P−Co_4N/CNW/CC, Co_4N/CC, and CNW/CC. (c) Polarization curves of Co_4N/CNW/CC before and after 1000 potential cycles. (d) Chronoamperometric response at a constant potential of 1.54 V of Co_4N/CNW/CC in comparison to that of P−Co_4N/CNW/CC. (e) ORR polarization curves of Co_4N/CNW/CC, P−Co_4N/CNW/CC, Co_4N/CC, and CNW/CC (in an O_2-saturated 1 M KOH solution). (f) Chronoamperometric response at a constant potential of 0.5 V of Co_4N/CNW/CC and P−Co_4N/CNW/CC in an O_2-saturated 1 M KOH solution.

Co_4N/CNW/CC is also directly used as the working electrode for the measurements toward ORR. Higher onset potential is achieved for Co_4N/CNW/CC. The Co_4N/CNW/CC exhibits a half-wave potential ($E_{1/2}$) of 0.80 V (Figure 2e). In contrast, the $E_{1/2}$ for P−Co_4N/CNW/CC, Co_4N/CC, and CNW/CC is 0.73, 0.79, and 0.41 V, respectively. Co_4N/CNW/CC has much higher current density of −16.5 mA cm^{-2} at the potential of 0.2 V than that of Co_4N/CC (−7.04 mA cm^{-2}), meaning more ORR active sites, which should be attributed to assistance of PPy-derived N-doped carbon fibers, and the high current density of −12.35 mA cm^{-2} for CNW/CC may prove it. As well as the OER measurements, the Co_4N/CNW/CC treated at 700 °C exhibits the best activity (Figure S18). After

DOI: 10.1021/jacs.6b05046
J. Am. Chem. Soc. 2016, 138, 10226−10231

acid corrosion of Co_4N, more ORR active sites are exposed. As shown in Figure S19, the Co_4N/CNW/CC-A displays better activity with more positive onset and half-wave potential for ORR, but much worse OER performance. Recent studies demonstrated that SCN^- ions can generally poison the metal−N−C catalyst. After treatment with SCN^- as Jiang[18] and co-workers did, both Co_4N/CNW/CC and Co_4N/CNW/CC-A suffer from decline activity for ORR (Figure S20), which undoubtedly indicates the Co−N−C active sites for ORR and Co_4N for OER in Co_4N/CNW/CC. The overall oxygen electrode activity can be evaluated by the difference of OER and ORR metrics ($\Delta E = E_{j=10} - E_{1/2}$). The Co_4N/CNW/CC exhibits a ΔE value of 0.74 V, corroborating the excellent reversible oxygen electrode nature of Co_4N/CNW/CC. The chronoamperometric response in Figure 2f displays a nearly constant current density within 20 h compared to P−Co_4N/CNW/CC, which reveals a stronger durability of Co_4N/CNW/CC for ORR. Furthermore, the Co_4N/CNW/CC exerts higher ORR activity and stability compared to commercial Pt/C (Figure S21).

Considering the excellent bifunctional catalytic activity of Co_4N/CNW/CC for ORR and OER, a conventional Zn−air battery is assembled to further identify its performance under real battery operation conditions. For comparison, the P−Co_4N/CNW/CC and Pt/C are also tested under the same conditions. An open-circuit voltage of ca. 1.4 V is observed for the battery with a Co_4N/CNW/CC cathode. The discharge polarization curves and peak power density of each single battery presented in Figure 3b clearly reveal that the Co_4N/CNW/CC cathode has the highest power density of 174 mW cm^{-2} compared to P−Co_4N/CNW/CC (135 mW cm^{-2}) and Pt/C (122 mW cm^{-2}). The galvanostatic discharge curves (Figure S22) display that the Co_4N/CNW/CC cathode possesses the specific capacities of 774 and 701 mAh g^{-1} (normalized to the mass of consumed Zn) at current densities of 10 and 50 mA cm^{-2}, respectively. We further investigate the rechargeable Zn−air batteries; the electrolyte used is 6 M KOH with 0.2 M Zn acetate to ensure reversible Zn electrochemical reactions at the anode. Figure 3c shows typical discharging and charging polarization curves, the whole charging and discharging overpotential of Co_4N/CNW/CC is 1.09 V at a current density of 50 mA cm^{-2} lower than that of P−Co_4N/CNW/CC (1.31 V) and Pt/C (1.47 V). Figure 4f presents typical cycling results; the initial discharge and charge voltages

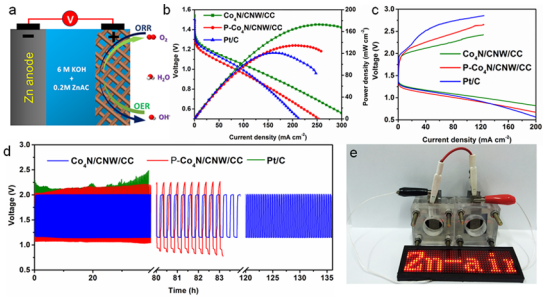

Figure 3. (a) Scheme of the Zn−air battery. (b) Battery voltage and power density of Zn−air batteries with Co_4N/CNW/CC, P−Co_4N/CNW/CC, and Pt/C as cathodes. (c) Charge and discharge polarization curves. (d) Galvanostatic discharge−charge cycling curves at 10 mA cm^{-2} of rechargeable Zn−air batteries with the Co_4N/CNW/CC electrode P−Co_4N/CNW/CC and Pt/C catalyst on carbon cloth, respectively. (e) Photograph of a small red LED panel powered by two Zn−air batteries with the Co_4N/CNW/CC electrode connected in series.

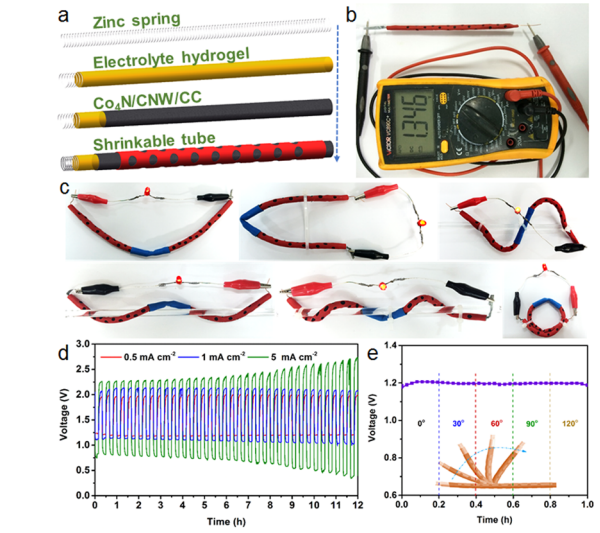

Figure 4. (a) Schematic illustration of the fabrication and structure characterization of the cable-type Zn−air battery. (b) Photograph of the cable-type Zn−air battery with an open-circuit voltage of 1.346 V. (c) Photograph of the cable-type Zn−air battery at various bended and twisted conditions. (d) Galvanostatic discharge−charge cycling curves at 0.5, 1, and 5 mA cm^{-2}. (e) Discharge curves at a current density of 0.5 mA cm^{-2} by bending to 30, 60, 90, and 120° every 12 min.

are about 1.16 and 2.00 V at a current density of 10 mA cm^{-2} at 20 min per cycle, respectively, and the voltage gap is only about 0.84 V. The voltage maintains very well for both discharge and charge; no visible change is observed even after continuous cycling of more than 136 h (up to 408 cycles). The rechargeable Zn−air battery with a Pt/C or P−Co_4N/CNW/CC cathode coated on a carbon cloth shows notable changes in both discharge and charge voltage.

Inspired by the excellent flexible property of Co_4N/CNW/CC electrode and stimulated by the increasing interests on portable and wearable electronic devices in recent years, a flexible rechargeable cable-type Zn−air battery is fabricated. Figure 4a shows the schematic fabrication of the rechargeable cable-type Zn−air battery. A narrow Zn belt is first coiled onto a steel rod forming a spring structure, followed by removing the rod. Then, the Zn spring is coated with a hydrogel polymer electrolyte solution. After the above step, the Co_4N/CNW/CC electrode is winded on the surrounding of the Zn spring shrouded in hydrogel. Finally, a punched heat-contraction rubber cable is used to pack the electrode assembly. As shown in Figure 4b, a high open-circuit voltage (OCV) of 1.346 V is obtained. To investigate their flexibility, the as-fabricated cable-type Zn−air batteries are intentionally bended and twisted into different shapes; surprisingly, it can be found that red light-emitting diode remains constantly powered under all the testing conditions (Figure 4c). Galvanostatic discharge measurements are conducted at different current densities to study the stability. The galvanostatic discharge curves in Figure S23 indicate that the Co_4N/CNW/CC cathode shows a voltage plateau of ~1.23 V at a current density of 0.5 mA cm^{-2} and a standing time as long as 15 h. With increasing current density to 1.0 mA cm^{-2}, the duration time decreases to 8 h almost linearly. This cable-type Zn−air battery reveals perfect rechargeable performance. Thirty-six discharge/charge cycles

DOI: 10.1021/jacs.6b05046
J. Am. Chem. Soc. 2016, 138, 10226−10231

for about 12 h are realized at a constant current density of 0.5 mA cm^{-2} (20 min per cycle), and the charge−discharge voltage plateau is maintained very well. Even at higher current densities of 1 and 5 mA cm^{-2}, our cable-type Zn−air battery still has stable cycles. The discharge performance is further compared before and after bending (bent at 30, 60, 90, and 120°); as shown in Figure 4d, the discharge voltage remains almost unchanged at a current density of 0.5 mA cm^{-2} under shape change. The Nyquist plots of impedance measured at 1.0 V under different bending conditions (Figure S24) display that the charge-transfer resistances (R_{ct}) are almost identical (≈17 Ω) under various bending conditions. Furthermore, to confirm whether the mechanical stress would degrade the electrochemical performance of cable-type flexible Zn−air battery, they are first repeated bended and stretched for thousands of times. Surprisingly, even after 2000 cycles of bending/stretching, the discharge curve only suffers from a very slight drop of ∼13 mV (Figure S25), showing high mechanical stability of the flexible cable-type Zn−air battery.

3. CONCLUSIONS

In summary, a 3D free-standing bifunctional oxygen electrode is first successfully developed, through one-step carbonization of a string of ZIF-67 on polypyrrole nanofibers network rooted on carbon cloths under a N_2 atmosphere. Homogeneous Co_4N nanoparticles, carbon species, and in situ formed Co−N−C active sites uniformly disperse along the in situ conversed N-doped carbon nanofibers network. Benefiting from the highly active sites, large special surface area, and 3D network structure, the Co_4N/CNW/CC electrode shows excellent catalytic performance for OER and ORR, which ensures an exceptionally high performance for both primary and rechargeable Zn−air batteries. Furthermore, the Co_4N/CNW/CC electrode-based cable-type Zn−air battery displays excellent rechargeable performance at a high current density of 0.5 and 1 mA cm^{-2}; the flexible characteristics give it a huge potential for wearable electronic devices. The developed free-standing reversible oxygen electrode might open new avenues for advanced catalytic applications such as water-splitting devices and other key renewable energy systems.

■ ASSOCIATED CONTENT

Supporting Information

The Supporting Information is available free of charge on the ACS Publications website at DOI: 10.1021/jacs.6b05046.

Experimental details, SEM and TEM images, and crystalline structure of the ZIF-67/PNW/CC, XPS, and N_2 adsorption of Co_4N/CNW/CC (PDF)

■ AUTHOR INFORMATION

Corresponding Author

*xbzhang@ciac.ac.cn.

Author Contributions

All authors have given approval to the final version of the manuscript.

Notes

The authors declare no competing financial interest.

■ ACKNOWLEDGMENTS

This work is financially supported by National Program on Key Basic Research Project of China (973 Program, Grant No. 2012CB215500), National Natural Science Foundation of China (21422108, 21271168 and 51472232) and Strategic Priority Research Program of the Chinese Academy of Sciences (Grant No. XDA09010404).

■ REFERENCES

(1) (a) Liu, Z.; Xu, J.; Chen, D.; Shen, G. Z. *Chem. Soc. Rev.* **2015**, *44*, 161−192. (b) Li, L.; Wu, Z.; Yuan, S.; Zhang, X. B. *Energy Environ. Sci.* **2014**, *7*, 2101−2122. (c) Li, N.; Chen, Z. P.; Ren, W. C.; Li, F.; Cheng, H. M. *Proc. Natl. Acad. Sci. U. S. A.* **2012**, *109*, 17360−17365.

(2) (a) Hu, L.; Cui, Y. *Energy Environ. Sci.* **2012**, *5*, 6423−6435. (b) De Volder, M. F.; Tawfick, S. H.; Baughman, R. H.; Hart, A. J. *Science* **2013**, *339*, 535−539. (c) Xu, Y.; Zhang, Y.; Guo, Z.; Ren, J.; Wang, Y.; Peng, H. *Angew. Chem., Int. Ed.* **2015**, *54*, 15390−15394.

(3) (a) Li, Y.; Dai, H. J. *Chem. Soc. Rev.* **2014**, *43*, 5257−5275. (b) Cheng, F. Y.; Chen, J. *Chem. Soc. Rev.* **2012**, *41*, 2172−2192. (c) Liu, X.; Park, M.; Kim, M. G.; Gupta, S.; Wang, X.; Wu, G.; Cho, J. *Nano Energy* **2016**, *20*, 315−325. (d) Park, J.; Park, M.; Nam, G.; Lee, J.; Cho, J. *Adv. Mater.* **2015**, *27*, 1396−1401.

(4) (a) He, W.; Jiang, C.; Wang, J.; Lu, L. *Angew. Chem., Int. Ed.* **2014**, *53*, 9503−9507. (b) Cheon, J. Y.; Kim, J. H.; Kim, J. H.; Goddeti, K. C.; Park, J. Y.; Joo, S. H. *J. Am. Chem. Soc.* **2014**, *136*, 8875−8878. (c) Fominykh, K.; Feckl, J. M.; Sicklinger, J.; Döblinger, M.; Böcklein, S.; Ziegler, J.; Peter, L.; Rathousky, J.; Scheidt, E. W.; Bein, T.; Rohlfing, D. F. *Adv. Funct. Mater.* **2014**, *24*, 3123−3129.

(5) (a) Chang, S. T.; Wang, C. H.; Du, H. Y.; Hsu, H. C.; Kang, C. M.; Chen, C. C.; Wu, J. C. S.; Yen, S. C.; Huang, W. F.; Chen, L. C.; Lin, M. C.; Chen, K. H. *Energy Environ. Sci.* **2012**, *5*, 5305−5314. (b) Trotochaud, L.; Young, S. L.; Ranney, J. K.; Boettcher, S. W. *J. Am. Chem. Soc.* **2014**, *136*, 6744−6753. (c) Takeguchi, T.; Yamanaka, T.; Takahashi, H.; Watanabe, H.; Kuroki, T.; Nakanishi, H.; Orikasa, Y.; Uchimoto, Y.; Takano, H.; Ohguri, N.; Matsuda, M.; Murota, T.; Uosaki, K.; Ueda, W. *J. Am. Chem. Soc.* **2013**, *135*, 11125−11130. (d) Reier, T.; Oezaslan, M.; Strasser, P. *ACS Catal.* **2012**, *2*, 1765−1772.

(6) Gorlin, Y.; Jaramillo, T. F. *J. Am. Chem. Soc.* **2010**, *132*, 13612−13614.

(7) Liu, Q.; Jin, J.; Zhang, J. *ACS Appl. Mater. Interfaces* **2013**, *5*, 5002−5008.

(8) Tian, G. L.; Zhao, M. Q.; Yu, D.; Kong, X. Y.; Huang, J. Q.; Zhang, Q.; Wei, F. *Small* **2014**, *10*, 2251−2259.

(9) (a) Yuan, S.; Huang, X. L.; Ma, D. L.; Wang, H. G.; Meng, F. Z.; Zhang, X. B. *Adv. Mater.* **2014**, *26*, 2273−2279. (b) Sun, L.; Li, M.; Jiang, Y.; Kong, W.; Jiang, K.; Wang, J.; Fan, S. *Nano Lett.* **2014**, *14*, 4044−4049. (c) Luo, S.; Wang, K.; Wang, J.; Jiang, K.; Li, Q.; Fan, S. *Adv. Mater.* **2012**, *24*, 2294−2298. (d) Tong, S.; Zheng, M.; Lu, Y.; Lin, Z.; Zhang, X.; He, P.; Zhou, H. *Chem. Commun.* **2015**, *51*, 7302−7304.

(10) (a) Liu, B.; Zhang, J.; Wang, X.; Chen, G.; Chen, D.; Zhou, C.; Shen, G. *Nano Lett.* **2012**, *12*, 3005−3011. (b) Long, J. W.; Dunn, B.; Rolison, D. R.; White, H. S. *Chem. Rev.* **2004**, *104*, 4463−4492. (c) Lahiri, I.; Oh, S. W.; Hwang, J. Y.; Cho, S.; Sun, Y. K.; Banerjee, R.; Choi, W. *ACS Nano* **2010**, *4*, 3440−3446. (d) Li, B.; Ge, X. M.; Goh, F. W. T.; Hor, T. S. A.; Geng, D. S.; Du, G. J.; Liu, Z. L.; Zhang, J.; Liu, X. G.; Zong, Y. *Nanoscale* **2015**, *7*, 1830−1838.

(11) Chen, P.; Xu, K.; Fang, Z.; Tong, Y.; Wu, J.; Lu, X.; Peng, X.; Ding, H.; Wu, C. Z.; Xie, Y. *Angew. Chem., Int. Ed.* **2015**, *54*, 14710−14714.

(12) (a) Zhang, G.; Xia, B. Y.; Wang, X.; Lou, X. W. D. *Adv. Mater.* **2014**, *26*, 2408−2412. (b) Xu, J.; Gao, P.; Zhao, T. S. *Energy Environ. Sci.* **2012**, *5*, 5333−5339. (c) Liu, X.; Chang, Z.; Luo, L.; Xu, T.; Lei, X.; Liu, J.; Sun, X. *Chem. Mater.* **2014**, *26*, 1889−1895. (d) Zhu, H.; Zhang, S.; Huang, Y. X.; Wu, L.; Sun, S. *Nano Lett.* **2013**, *13*, 2947−2951.

(13) (a) Cao, B.; Veith, G. M.; Neuefeind, J. C.; Adzic, R. R.; Khalifah, P. G. *J. Am. Chem. Soc.* **2013**, *135*, 19186−19192. (b) Sun, T.; Wu, Q.; Che, R.; Bu, Y.; Jiang, Y.; Li, Y.; Yang, L. J.; Wang, X. Z.;

Hu, Z. *ACS Catal.* **2015**, *5*, 1857−1862. (c) Ito, K.; Harada, K.; Toko, K.; Akinaga, H.; Suemasu, T. *J. Cryst. Growth* **2011**, *336*, 40−43.
(14) (a) Bezerra, C. W.; Zhang, L.; Lee, K.; Liu, H.; Marques, A. L.; Marques, E. P.; Wang, H.; Zhang, J. *Electrochim. Acta* **2008**, *53*, 4937−4951. (b) Niu, K.; Yang, B.; Cui, J.; Jin, J.; Fu, X.; Zhao, Q.; Zhang, J. *J. Power Sources* **2013**, *243*, 65−71. (c) Zhang, R.; He, S.; Lu, Y.; Chen, W. *J. Mater. Chem. A* **2015**, *3*, 3559−3567. (d) Liang, H. W.; Wei, W.; Wu, Z. S.; Feng, X.; Müllen, K. *J. Am. Chem. Soc.* **2013**, *135*, 16002−16005.
(15) (a) Wu, R.; Qian, X.; Rui, X.; Liu, H.; Yadian, B.; Zhou, K.; Wei, J.; Yan, Q.; Feng, X. Q.; Long, Y.; Wang, L.; Huang, Y. *Small* **2014**, *10*, 1932−1938. (b) You, B.; Jiang, N.; Sheng, M.; Gul, S.; Yano, J.; Sun, Y. *Chem. Mater.* **2015**, *27*, 7636−7642.
(16) Ibrahim, M.; Marcelot, G. C.; Atmane, K. A.; Berrichi, E.; Lacroix, L. M.; Zwick, A.; Fonrose, B. W.; Lachaize, S.; Decorse, P.; Piquemal, J. Y.; Viau, G. *J. Phys. Chem. C* **2013**, *117*, 15808−15816.
(17) (a) Chen, Y. Z.; Wang, C.; Wu, Z. Y.; Xiong, Y.; Xu, Q.; Yu, S. H.; Jiang, H. L. *Adv. Mater.* **2015**, *27*, 5010−5016. (b) Wei, J.; Hu, Y.; Wu, Z.; Liang, Y.; Leong, S.; Kong, B.; Zhang, X.; Zhao, D.; Simon, G. P.; Wang, H. *J. Mater. Chem. A* **2015**, *3*, 16867−16873. (c) Hou, Y.; Wen, Z.; Cui, S.; Ci, S.; Mao, S.; Chen, J. *Adv. Funct. Mater.* **2015**, *25*, 872−882.
(18) Jiang, W. J.; Gu, L.; Li, L.; Zhang, Y.; Zhang, X.; Zhang, L. J.; Wang, J. Q.; Hu, J. S.; Wei, Z. D.; Wan, L. J. *J. Am. Chem. Soc.* **2016**, *138*, 3570−3578.

DOI: 10.1021/jacs.6b05046
J. Am. Chem. Soc. 2016, 138, 10226−10231